Orbital ordering and quasi-two-dimensional magnetism in $A\mathrm{MnF_4}$ (A = K, Rb): A first-principles study

Anuroopa Behatha,[1] Tulika Maitra,[2] Alexander N. Rudenko,[3] and V. Kanchana[1,*]

[1]*Department of Physics, Indian Institute of Technology Hyderabad, Kandi 502285, Sangareddy, Telangana, India*

[2]*Department of Physics, Indian Institute of Technology Roorkee, Roorkee 247667, Uttarakhand, India*

[3]*Institute for Molecules and Materials, Radboud University, 6525 AJ Nijmegen, Netherlands*

(Received 4 December 2021; revised 20 April 2022; accepted 17 June 2022; published 12 July 2022)

Strongly correlated systems with the interplay of electronic, charge, spin, and orbital degrees of freedom have, in recent times, received a surge of interest because of their rich physics, novel physical properties, and potential applications. In the present work, we study the structural, magnetic, and electronic properties and orbital ordering in layered perovskite-type $A\mathrm{MnF_4}$ (A=K, Rb) from first principles. A detailed analysis of the electronic properties in both compounds reveals an interesting nodal-line-like dispersion at ∼0.4 eV below the Fermi level at the hinges of the Brillouin zone. Magnetic properties reflect the quasi-two-dimensional magnetism in these compounds, with very weak exchange interaction between the layers. Our results report the robust in-plane ferromagnetic spin order in $A\mathrm{MnF_4}$ (A=K, Rb) with the critical temperatures estimated to be around 30–60 K. We also find an anti-ferro-orbital ordering within the *ab* plane and a ferro-orbital ordering out of plane favoring the *C*-type orbital order in these compounds.

DOI: 10.1103/PhysRevB.106.024409

I. INTRODUCTION

In condensed-matter physics, besides spin and charge, the orbital degrees of freedom and their interactions play a pivotal role in the correlated electronic system with its rich physics and novel phenomena such as the Kondo effect, heavy fermions, and colossal magnetoresistance [1,2]. Orbital ordering is defined to be the spatial arrangement of different orbitals in a manner similar to that of the ordered arrangement of magnetic spins in magnetic materials. Great advances regarding its origin have been made in the field of orbital physics both experimentally and theoretically [3–6]. Orbital ordering, in particular, plays a key role in multi-orbital structured materials like transition metal oxides.

Transition metal oxides are one of the celebrated compounds with rich physics and extensive applications. Some key factors for a plethora of such intriguing phenomena are the type of atomic ion present, the availability of degenerate orbitals in the system, and the crystallographic surrounding. Perovskite-based manganites set a well-known example for such studies. In particular, manganese oxides have attracted a lot of interest because of the presence of colossal magnetoresistance [1,7], a phenomenon which is most relevant to the orbital ordering [8–10] and correlation effects. In particular, $\mathrm{LaMnO_3}$, which is a well-known colossal magnetoresistance manganite, is interesting due to the presence of the cooperative Jahn-Teller (JT) distortion accompanied by antiferromagnetic (AFM) spin ordering and *C*-type orbital ordering in it [11]. In addition to the transition metal oxides, fluoride-based compounds also display interesting structural, electronic and magnetic properties [12–14]. The compound of interest in this work, $A\mathrm{MnF_4}$ (A=K, Rb), which is a perovskite-type structure with the JT active ion Mn^{3+} ($3d^4$), motivated us to study the existence of orbital ordering in it. These alkalitetraflouromanganates crystallize in monoclinic symmetry with space group $P2_1/a$ and resemble the related layered structure $\mathrm{TlAlF_4}$ [15,16]. Moron *et al.* initially reported $\mathrm{RbMnF_4}$ stabilizes in an orthorhombic cell with space group *Pmab* and later confirmed that it possesses a structure similar to that of $\mathrm{KMnF_4}$ [17]. Neutron diffraction experiments on $A\mathrm{MnF_4}$ (A=K, Rb) revealed different antiferromagnetic spin arrangements below Néel temperatures T_N = 4.5 and 2.3 K, respectively [18–20]. In the present work, the theoretical analysis of the electronic band structure, magnetic properties, and orbital ordering of the series $A\mathrm{MnF_4}$ (where A=K, Rb) was carried out using density functional theory (DFT). From the crystal structure point of view and by analyzing the magnetic properties, it is quite evident that these compounds form an ideal platform for two-dimensional (2D) models due to the presence of weak interactions between the adjacent layer of $\mathrm{MnF_6}$ octahedra.

The outline of this work is as follows. The computational methods used here are given in Sec. II. Following that, a discussion of the magnetic and electronic properties along with an analysis of the orbital ordered ground states of $A\mathrm{MnF_4}$ (A=K, Rb) are given in Sec. III. Finally, we conclude our results in Sec. IV.

II. COMPUTATIONAL DETAILS

First-principles calculations were carried out to compute the electronic band structure, magnetic properties, and orbital ordering phenomena within an accurate projected augmented

*kanchana@iith.ac.in

wave (PAW) [21] method as implemented in the Vienna Ab initio Simulation Package (VASP) [22,23]. Experimentally, AMnF$_4$ (A=K, Rb) is reported to possess noncollinear and collinear AFM magnetic order [17]. To explain the ground state of the system, we carried out full geometrical optimization of these compounds, and the resulting parameters are given in Tables IV and V (see the Appendix). Our calculations reveal the ferromagnetic (FM) order in both compounds. We proceeded further with experimental lattice parameters (i.e., by relaxing the atomic positions alone) with a k mesh of $6 \times 6 \times 8$ to sample the irreducible Brillouin zone and a large energy cutoff of 520 eV for a plane-wave basis set to attain a ground state on par with experiments. When the force between the atoms reaches 0.01 eV/Å with a total energy tolerance of 10^{-6} eV, self-consistency is achieved. The valence configurations used throughout the calculations were $3s^2 3p^6 4s^1$, $4s^2 4p^6 5s^1$, $4s^2 3d^5$, and $2s^2 2p^5$ for K, Rb, Mn, and F respectively. The presence of Mn d electrons demands better accounting of electron correlations in these compounds. To enable the localization of Mn d electrons, we utilized the Perdew-Burke-Ernzerhof (PBE) + U method by including the effective Hubbard U parameter using the Dudarev approach [24] and found that the local Coulomb interactions have negligible effects on the observed ground state and the electronic band profile (details are given in the Appendix, Figs. 12 and 13) of the compounds. Spin-orbit coupling was included at the level of the scalar relativistic PAW pseudopotentials. We performed both collinear and noncollinear calculations in different magnetic spin configurations to identify the ground state of the system. The FM ground state of the system and the calculated exchange interactions were tested for convergence with respect to the k-point mesh and the plane-wave energy cutoff values (see Fig. 10 in the Appendix).

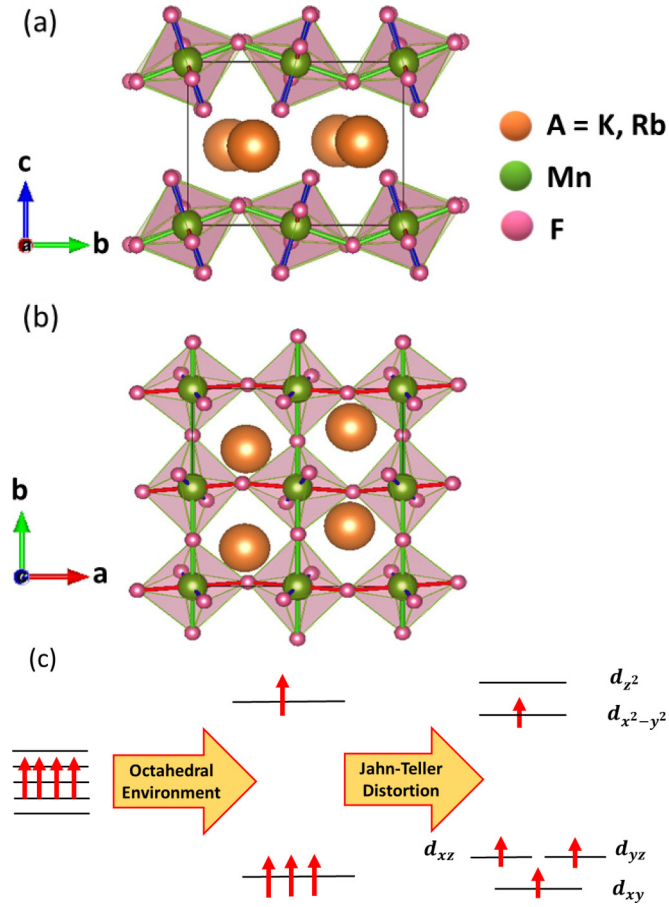

FIG. 1. Crystal structure of AMnF$_4$ in $P2_1/a$ space group (No. 14) with (a) side and (b) top views of the unit cell. Orange, green, and pink spheres represent K, Mn, and F, respectively. (c) Schematic illustration of energy-level splitting in AMnF$_4$ in an octahedral crystal environment surrounding a "Mn" atom.

III. RESULTS AND DISCUSSION

A. Crystal structure and magnetic properties

AMnF$_4$ (A=K, Rb) belongs to the family of layered perovskites and has the same monoclinic symmetry with space group $P2_1/n$ (No. 14), with 24 atoms in the primitive cell (i.e., 4 f.u.). As shown in Fig. 1, AMnF$_4$ forms a sandwichlike structure with the presence of a MnF$_6$ corner-sharing octahedral arrangement separated along the c axis by the K/Rb atoms. In 1993, Moron *et al.* [17] reported the experimental parameters along with their atomic positions, which are (in Å) $a = 7.6830$ (7.7865), $b = 7.6290$ (7.7447), and $c = 5.7444$ (5.9968) for KMnF$_4$ (RbMnF$_4$). We have fixed the experimental parameters and optimized the atomic positions under the generalized gradient approximation (GGA) PBE scheme. The structural parameters are summarized in Table I.

The crystal symmetries (besides the translations) present in the following compounds are the horizontal glide mirror G_z, $(x, y, z) \rightarrow (x + 1/2, -y + 1/2, z)$; screw axis, $(x, y,$

TABLE I. Details of the experimental lattice parameters along with the calculated bond lengths and bond angles for AMnF$_4$ (A=K, Rb). Mn-F$_{ax}$ refers to the axial bond length, whereas Mn-F$_{eq}$ (a) and Mn-F$_{eq}$ (b) correspond to the equatorial bond lengths along the a and b axes, respectively.

	a (Å)	b (Å)	c (Å)	Mn-F$_{ax}$ (Å)	Mn-F$_{eq}$ (a) (Å)	Mn-F$_{eq}$ (b) (Å)	Mn-F$_{eq}$-Mn (deg)
KMnF$_4$	7.68	7.63	5.74	1.81[a]	2.10[a]	1.92[a]	146.37[b]
				1.81[c]	1.91[c]	2.13[c]	140.11[d]
RbMnF$_4$	7.79	7.74	5.99	1.80[a]	2.11[a]	1.96[a]	150.32[b]
				1.82[c]	1.92[c]	2.09[c]	145.50[d]

[a]Mn(0,0,0) octahedron.
[b]Mn-F-Mn angle along the a axis.
[c]Mn(0, 1/2, 0) octahedron.
[d]Mn-F-Mn angle along the b axis.

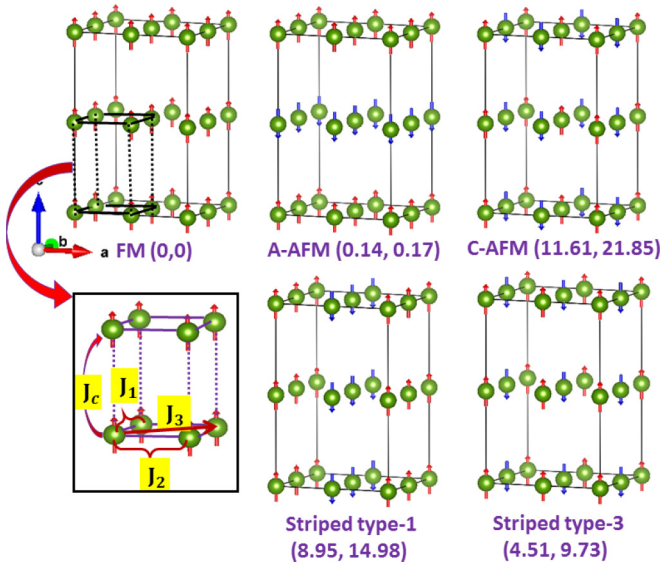

FIG. 2. Schematic model representing the Mn spin moments in various magnetic configurations used for calculating the exchange constants. J_1, J_2, and J_3 are the intraplanar nearest-neighbor exchange coupling constants, and J_c is the interplanar nearest-neighbor exchange coupling constant. For $KMnF_4$ and $RbMnF_4$, the total energy differences of different magnetic configurations (meV/f.u.) relative to the FM ground state are presented in parentheses.

$z) \rightarrow (-x + 1/2, y + 1/2, -z)$; and the inversion symmetry P. With the presence of magnetic ordering, the time-reversal symmetry T would be broken. The structural stability of these $AMnF_4$ compounds has been verified by computing the cohesive energy/atom, which is -2.62 eV for $AMnF_4$ (A=K, Rb). These negative energy values confirm the stability of these systems.

To understand the ground state magnetic properties, we have simulated different magnetic spin configurations in collinear and noncollinear regimes using the DFT approach. The collinear magnetic spin alignments include FM, A-AFM, C-AFM, and two striped-type AFM states, as shown in Fig. 2. By comparing the energies of the different magnetic orders under the PBE+U scheme, we found that $AMnF_4$ (A=K, Rb) stabilizes in FM order, with the individual magnetic moment values listed in Table II. Following previous works [25–27], in most of the cases considered, we have fixed $U_{\text{eff}} = U - J$ to be 3 eV to treat $3d$ Mn electrons using the Dudarev approach

TABLE II. Magnetic moments (in units of μ_B) of Mn as a function of the parameter U.

	$U = 3$ eV		$U = 5$ eV	
	Orbital	Spin	Orbital	Spin
$KMnF_4$				
GGA+U		3.787		3.873
GGA+U+SOC	−0.005	3.784	−0.006	3.868
$RbMnF_4$				
GGA+U		3.805		3.891
GGA+U+SOC	−0.005	3.801	−0.006	3.883

TABLE III. Details of the simulated exchange constants and the calculated mean-field (T_c^{MFA}) and random-phase (T_c^{RPA}) critical temperatures at different Hubbard parameters (i.e., $U = 3$, 5 eV) using PAW methods.

	U_{eff} (eV)	J_1 (meV)	J_2 (meV)	J_3 (meV)	J_c (meV)	T_c^{MFA} (K)	T_c^{RPA} (K)
$KMnF_4$	3	0.448	1.003	0.057	0.018	73.29	31.8
	5	0.475	0.924	0.029	0.019	69.49	29.8
$RbMnF_4$	3	1.037	1.694	0.089	0.021	135.79	56.5
	5	0.942	1.476	0.050	0.020	117.73	49.0

[24]. In some cases, we also used $U_{\text{eff}} = 5$ eV for comparative purposes.

Further, we have included spin-orbit coupling (SOC) in both the compounds in order to compute the magnetocrystalline anisotropy energy (MAE) by aligning magnetic moments in different directions (i.e., along [100], [010], [001], [110], [011], and [101]). We found that the preferred direction of magnetization (easy axis) is along [100] for $KMnF_4$ and [110] for $RbMnF_4$, whereas the hard axis corresponds to [001] for both compounds. The energy difference between [100] and [110] is of the order of μeV, implying that the in-plane directions of magnetization are nearly degenerate. The resulting MAE is found to be 0.58 meV/f.u. for $KMnF_4$ and 0.54 meV/f.u. for $RbMnF_4$. Considering that the energy difference between different magnetization directions is small, we continue our further magnetic and electronic structure analysis with the magnetization direction along [001].

The exchange interactions can be estimated by mapping the DFT total energies of each spin configuration to the underlying Heisenberg spin model,

$$H = -\frac{1}{2}\sum_{ij} J_{ij}\mathbf{S}_i\mathbf{S}_j, \tag{1}$$

where J_{ij} is the exchange interaction between sites i and j and $\mathbf{S}_{i(j)}$ is the corresponding spin.

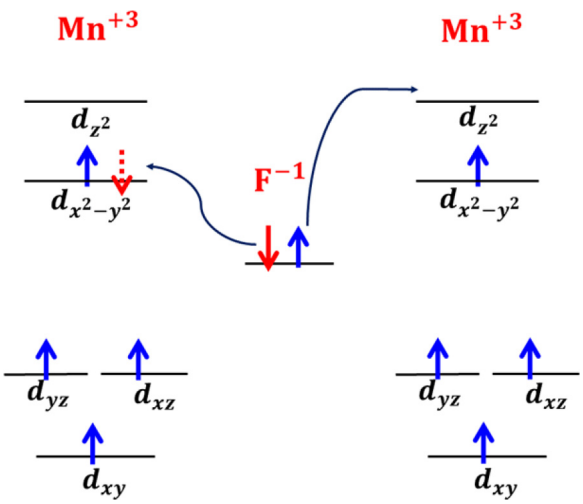

FIG. 3. Schematic representation of superexchange phenomena between Mn and F ions leading to FM order in $AMnF_4$ (A=K, Rb).

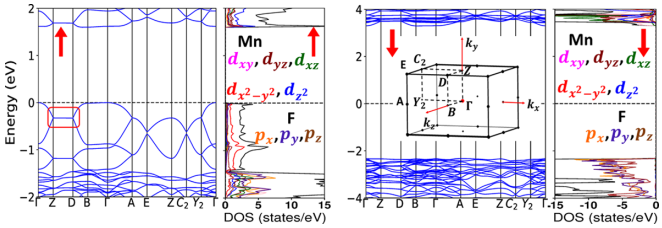

FIG. 4. Spin-polarized electronic band structure of $KMnF_4$ along the high-symmetry points as indicated in the irreducible Brillouin zone (shown in the inset) and the partial density of states (DOS) highlighting the predominant contribution of Mn d and F p states close to the Fermi level E_F. Left: spin-up channel. Right: spin-down channel.

Figure 2 depicts the various magnetic configurations used to calculate the exchange constants. The total energies for 8 f.u. can be stated as follows using the Heisenberg Hamiltonian for all magnetic configurations:

$$\begin{aligned} F &= E_N - 8J_1S^2 - 8J_2S^2 - 8J_cS^2 - 16J_3S^2, \\ A &= E_N - 8J_1S^2 - 8J_2S^2 + 8J_cS^2 - 16J_3S^2, \\ C &= E_N + 8J_1S^2 + 8J_2S^2 - 8J_cS^2 - 16J_3S^2, \\ S_1 &= E_N - 8J_1S^2 + 8J_2S^2 - 8J_cS^2 + 16J_3S^2, \\ S_3 &= E_N + 8J_1S^2 - 8J_2S^2 - 8J_cS^2 + 16J_3S^2, \end{aligned} \tag{2}$$

where E_N, F, A, C, S_1, and S_3 represent the energies of the nonmagnetic, FM, A-AFM, C-AFM, and two striped AFM-type configurations, respectively. The relevant exchange constants (J_1, J_2, J_3) are the first-, second-, and third-nearest-neighbor intraplanar exchange coupling constants, and J_c is the interplanar exchange coupling constant, as illustrated in Fig. 2. These exchange constants can be obtained from Eq. (2) using

$$\begin{aligned} J_1 &= -\frac{1}{32S^2}[F - C + S_1 - S_3], \\ J_2 &= -\frac{1}{32S^2}[F - C - S_1 + S_3], \\ J_3 &= -\frac{1}{64S^2}[F + C - S_1 - S_3], \\ J_c &= -\frac{1}{16S^2}[F - A], \end{aligned} \tag{3}$$

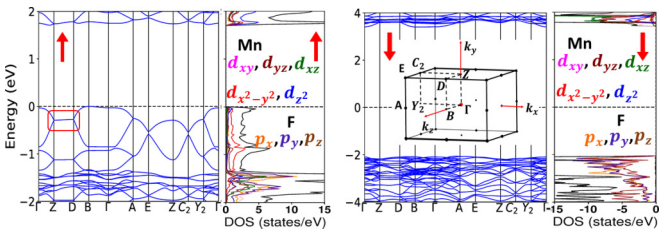

FIG. 5. Spin-polarized electronic band structure of $RbMnF_4$ along the high-symmetry points as indicated in the irreducible Brillouin zone (shown in the inset) and the partial DOS highlighting the predominant contribution of Mn d and F p states close to the Fermi level E_F. Left: spin-up channel. Right: spin down channel.

where we assume $S = 2$, in accordance with the calculated magnetic moment per Mn ion.

Next, we proceed to find these exchange constants with Hubbard U parameters ($U_{\text{eff}} = 3$ and 5 eV) and the values are listed in Table III. The close difference in energies of the FM and A-AFM magnetic configurations (see Fig. 2) justifies the smallness of the interplanar coupling J_c, as shown in Eq. (3).

Positive exchange interactions indicate that a FM coupling is favored in both compounds. The intraplanar couplings (i.e., J_1 and J_2) between the Mn ions being strongest when compared to the negligible interplanar coupling (i.e., J_c) intuitively suggests the possibility of quasi-2D magnetism in these layered magnetic materials.

The critical (Curie) temperature can be estimated using the mean-field expression [28] as

$$T_c = \frac{S(S+1)}{3k_B}\left(\sum_i z_i J_i\right), \tag{4}$$

where k_B is the Boltzmann constant and z_i represents the number of nearest neighbors corresponding to the exchange constants J_i. Here, $z_1 = 2$, $z_2 = 2$, and $z_3 = 4$ are the numbers of in-plane nearest neighbors, and $z_c = 2$ is the out-of-plane nearest neighbors. The obtained values are given in Table III, whereas in the experimental reports they have an antiferromagnetic ground state with corresponding Néel temperatures of $T_N = 4.5$ and 2.3 K [18–20]. Given the quasi-2D character of magnetism in these compounds, the mean-field T_c values could be significantly overestimated. Note that $T_c \sim \{\ln[J_c/(J_1 + J_2)]\}^{-1}$; that is, T_c logarithmically approaches zero in the case of vanishing interlayer coupling, in accordance with the Mermin-Wagner theorem [29].

A more accurate and consistent estimation of T_c can be obtained using Tyablikov's decoupling approximation (also known as the random-phase approximation) [30],

$$T_c = \frac{S(S+1)}{3Sk_B}\left(\frac{1}{N}\sum_{\mathbf{q}}\frac{1}{E(\mathbf{q})}\right)^{-1}. \tag{5}$$

Here, $E(\mathbf{q})$ is the spin-wave dispersion. Assuming noninteracting magnons, the spin-wave dispersion for a single-sublattice ferromagnet reads

$$E(\mathbf{q}) = S[J(\mathbf{0}) - J(\mathbf{q})], \tag{6}$$

where $J(\mathbf{q}) = \sum_{\mathbf{R}_{ij}} J(\mathbf{R}_{ij})e^{-i\mathbf{q}\mathbf{R}_{ij}}$ is the Fourier transform of the distance-dependent exchange interaction. According to the model depicted in Fig. 2, there are two types of nearest-neighbor in-plane interactions (J_1 and J_2) forming a square lattice, a next-nearest-neighbor in-plane interaction (J_3), and an interplane (chainlike) interaction (J_c). In this situation, we have

$$\begin{aligned} J(\mathbf{q}) = {} & 2J_1\cos(q_x) + 2J_2\cos(q_y) \\ & + 4J_3\cos(q_x)\cos(q_y) + 2J_c\cos(q_z), \end{aligned} \tag{7}$$

where q_x and q_y (q_z) are given in units of the lattice constants a^{-1} (c^{-1}). From Eq. (7), $J(0) = 2J_1 + 2J_2 + 4J_3 + 2J_c$. Substituting the exchange constants (J_1, J_2, J_3, J_c) calculated for $AMnF_4$ (A=K, Rb) from Eq. (3) given above, we numerically obtain T_c values from the random phase as given in Table III

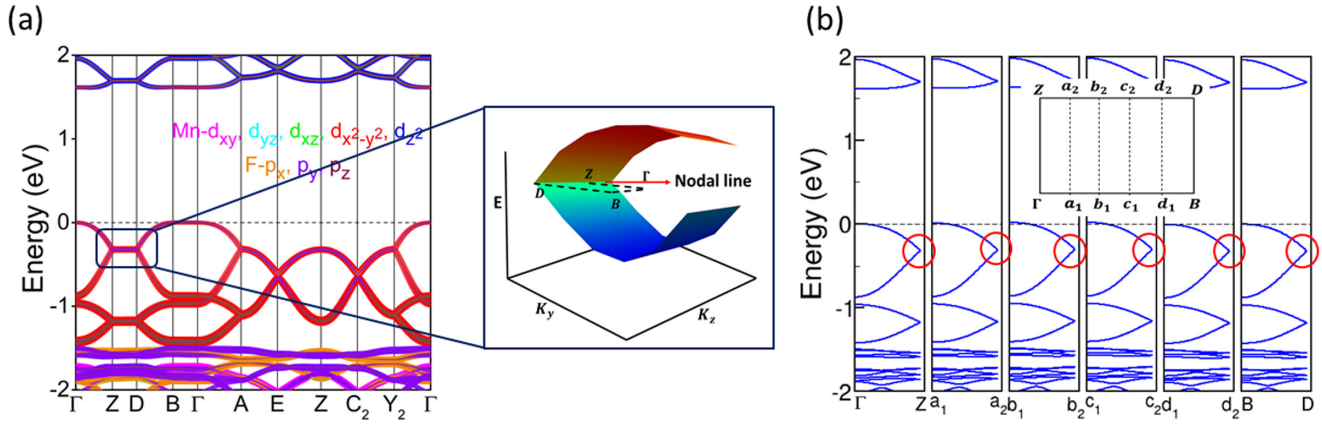

FIG. 6. (a) Calculated orbital-projected band structure in the spin-up channel for $KMnF_4$ along with the 3D band representation of the nodal line (highlighted in the blue box). (b) Illustration of the nodal line along the selected band paths between Γ-*Z* and *B*-*D* (i.e., along the $k_x = 0$ plane)

which are expectedly smaller compared to the mean-field estimate.

A schematic illustration of the superexchange pathway that leads to the possible magnetic ground state in $AMnF_4$ is presented in Fig. 3 using the semiempirical Goodenough-Kanamori-Anderson (GKA) rules [31–33]. According to the GKA rules, AFM coupling occurs when two half-filled cation orbitals interact, whereas FM coupling occurs when one half-filled and one empty cation orbitals interact [32]. Within the GKA picture, various factors that influence the sign and magnitude of the superexchange interaction between magnetic ions are (i) the bond angle between magnetic ions and the ligand, (ii) the crystal field environment, and (iii) the oxidation state of the magnetic ion. An alternative mechanism of superexchange interactions may be considered within the Kugel-Khomskii formalism [34], which results in a competition between AFM and FM interactions, originating from the multiorbital character of the *d* shell. While some orbitals couple antiferromagnetically, by following the GKA rules, the other orbitals may couple ferromagnetically [35]. The latter is strongly affected by the hybridization between the t_{2g} and e_g orbitals, as well as by the magnitude of the local Coulomb interactions and Hund's rule coupling. A detailed balance between these ingredients might be responsible for the FM ground state magnetic order in $KMnF_4$ and $RbMnF_4$, which warrants further refinement of experiments observing AFM ordering and might indicate insufficiency of our theory level, which motivates further studies.

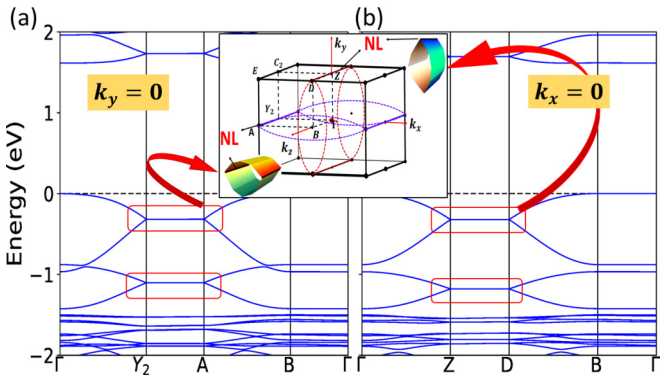

FIG. 7. (a) and (b) Calculated electronic band structures in spin-up states for $KMnF_4$ along the high-symmetry paths Γ-Y_2-*A*-*B*-Γ and Γ-*Z*-*D*-*B*-Γ (i.e., along the $k_y = 0$ and $k_x = 0$ planes, respectively) along with the schematic representation of the band profiles highlighting the nodal lines in the Brillouin zone.

B. Electronic properties

Let us now turn our attention towards the electronic properties of $AMnF_4$ (*A*=K, Rb). In Fig. 4, we provide the details of the spin-polarized band structure for $KMnF_4$ along with the partial density of states (PDOS) for FM magnetic order. We clearly observe that $KMnF_4$ behaves as a semiconductor in the spin-up channel (↑) with a band gap of 1.6 eV and as an insulator in the other spin channel (↓) with a large band gap of around 5 eV. Likewise, Fig. 5 illustrates the electronic band structure of $RbMnF_4$ along with the PDOS in its FM ground state, which are similar to those of $KMnF_4$ with a band gap of 1.8 eV in the spin-up channel and a large band gap of around 5 eV in the spin-down channel.

From the PDOS analysis in both compounds, we observe that it is Mn $d_{x^2-y^2}$ states that predominantly dominate at the valence states with a negligible contribution from the other Mn *d* states and F *p* states. When it comes to conduction bands, it is Mn d_{z^2} states that play a vital role with a negligible contribution from the other Mn *d* and F *p* states.

The band dispersions in both compounds are similar, and we spot some interesting features. First, we can see a flat band in the *B*-Γ direction at the valence band edge. This band gives rise to a Van Hove singularity in the DOS for both compounds. Next to that, $KMnF_4$ exhibits bands merging (see the left panel in Fig. 4) at the *Z* and *D* edges (in spin-up channel), ∼0.4 and ∼1.2 eV away from the Fermi level, which is reminiscent of a nodal-line-like dispersion along the path *Z*-*D*. Figure 6 displays the orbital-projected band structure along with the three-dimensional (3D) band dispersion depicting the nodal-line-like dispersion. After analyzing the band structure closely, we notice that this band merging is not an isolated

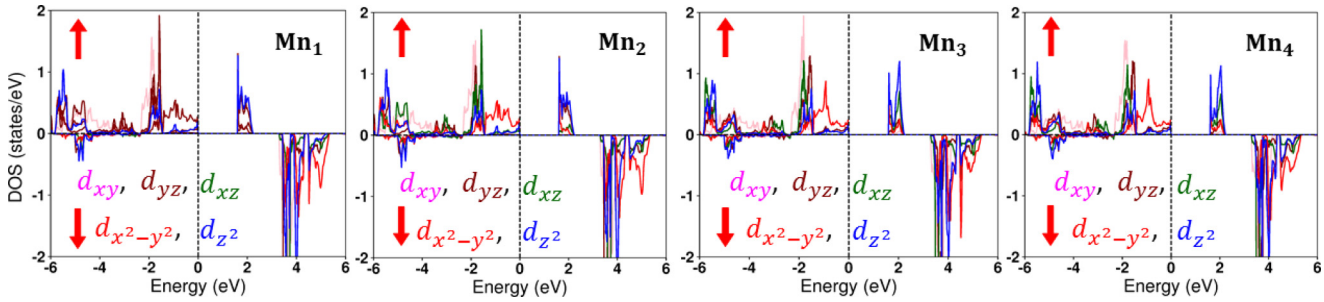

FIG. 8. Calculated partial DOS projected onto the 3*d* orbitals of four Mn ions in ground state $KMnF_4$ with the FM structure. The upward arrows (↑) indicate the spin-up channel, and the downward arrows (↓) indicate the spin-down channel.

point but, indeed, forms a continuous one-dimensional line, and hence, it is referred to as a nodal-line-like dispersion.

A schematic representation of the 2D plane in the Brillouin zone is given in the inset in Fig. 6(b). Due to the existence of a nodal line, we can expect a similar feature of bands merging on each k path in that plane, $k_x = 0$. To show this, we computed the band structures for the selected k paths in the $k_x = 0$ plane, which shows a similar crossing at the edges, thereby confirming the nodal-line dispersion along the path Z-D. The 3D band dispersion confirms the same and shows the nodal line along the path Z-D, as shown in Fig. 6.

Further, we analyzed the electronic band structures along different high-symmetry paths and found similar nodal-line-like dispersions along the high-symmetry path "Y_2A" (i.e., in $k_y = 0$ plane), ∼0.4 and ∼1.2 eV below E_F. Hence, we propose the existence of two nodal-line-like dispersions in each plane (i.e., $k_x = 0$ and $k_y = 0$). The electronic band structures along the $k_x = 0$ plane and $k_y = 0$ plane are shown in Fig. 7, highlighting the nodal-line-like dispersions along with the schematic representations of the band profile in the Brillouin zone (given in the inset).

In the case of Rb, we do observe a similar interesting band dispersion at edges Z and D, ∼0.4 and ∼1.2 eV below from the Fermi level that also features the nodal-line-like dispersion in the spin-up channel. In Fig. 15 in the Appendix, we provide the details of orbital-projected band structure along with the computed band structures for the selected k paths in the $k_x = 0$ plane, similar to how we proceeded for $KMnF_4$. Thus,

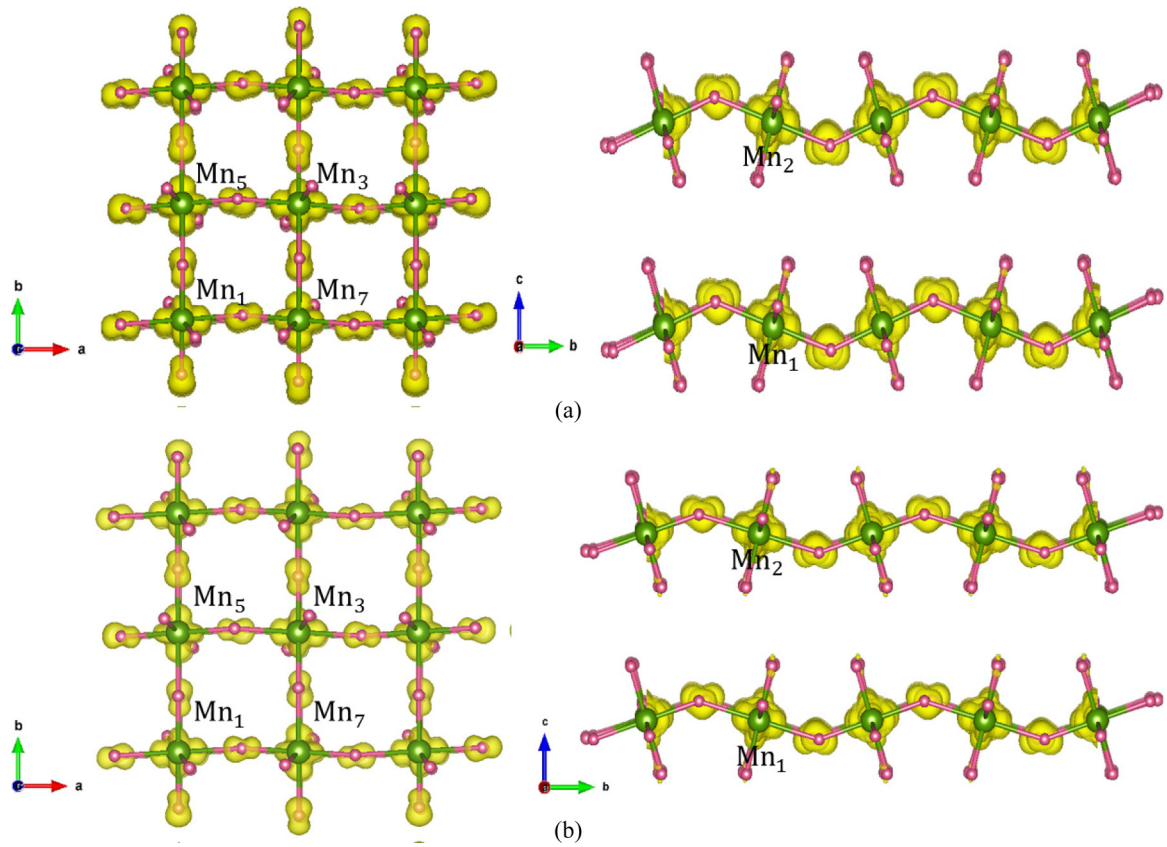

FIG. 9. Visualization of calculated charge density in real space in the region extending (a) from −1.8 eV to the Fermi level for $KMnF_4$ and (b) from −1.34 eV to the Fermi level for $RbMnF_4$. The charge densities highlight the $d_{x^2-y^2}$-like orbitals with the C-type orbital ordering.

$RbMnF_4$ is also believed to possess the interesting nodal-line-like dispersions situated slightly away from the Fermi level in the $k_x = 0$ and $k_y = 0$ planes.

Further, we computed the electronic band structures of these compounds by including SOC. Figure 11 in the Appendix, displays the computed band structures along with the PDOS for both compounds when SOC is included. From the band structure, we notice that these nodal-line-like dispersions are protected even in the presence of SOC. This case is similar to what we observed in our previous work on $CsMnF_4$ [36]. We also carried out our calculations with $U_{\text{eff}} = 5$ eV to check the effect of local Coulomb interactions over the electronic structure properties. We found negligible changes in the band profile in both compounds (details are provided in Figs. 12 and 13 in the Appendix). Band engineering (with doping/pressure) can induce shifts in the Fermi level to bring these nodal-line-like dispersions close to E_F, making these compounds viable in the field of nodal-line semimetals.

C. Orbital ordering

In order to identify the orbital ordering state present in the $A MnF_4$ series, we present the spin-polarized PDOS projected onto the d states of four individual Mn atoms for the case of $KMnF_4$, as shown in Fig. 8 (the details for $RbMnF_4$ are given in Fig. 14 in the Appendix). The octahedral environment around the Mn atoms allows the Mn d states to split into lower t_{2g} states (i.e., d_{xy}, d_{yz}, d_{xz}) and higher e_g (i.e., $d_{x^2-y^2}$, d_{z^2}) states. In $AMnF_4$, (A=K, Rb), we notice both tetragonal and trigonal distortions (which is a deviation of the F-Mn-F bond angle from 90°) in MnF_6 octahedron (refer to Table I for structural details). This local tetragonal distortion gives rise to compression along the z direction when compared to that of the ab plane. This compression of the MnF_6 octahedra along the c axis (i.e., the JT distortion), further lifts the degeneracy of t_{2g} into lower-energy d_{xy} and higher-energy d_{yz} and d_{xz}, whereas the e_g states split up into lower-energy $d_{x^2-y^2}$ and higher-energy d_{z^2} (see Fig. 1 for a schematic orbital diagram). In $AMnF_4$ (A=K, Rb), we see that the Mn lies in the +3 oxidation state ($3d^4$), with three of its electrons occupying lower t_{2g} levels and the fourth electron occupying the $d_{x^2-y^2}$ level. The same can be confirmed from the PDOSs provided in Figs. 4 and 5 (Left: spin up channel) for $KMnF_4$ and $RbMnF_4$, respectively, which highlights the predominant existence of Mn $d_{x^2-y^2}$ orbitals in the vicinity of the Fermi level.

To address the ground state orbital ordering in these two compounds, we analyze the 3D charge density for the valence states, as shown in Fig. 9. We notice an anti-ferro-orbital ordering of $d_{x^2-y^2}$-like orbitals within the ab plane with a ferro-orbital ordering out of plane (i.e., along the z direction), which confirms the C-type orbital ordering in these systems. From the Mn-F bond length analysis given in Table I, the Mn-F bond is elongated along the x direction and is compressed in the other directions, which might be the reason for the anisotropy observed in the orbital ordering along the a and b axes. From Fig. 9, it is evident that $AMnF_4$ (A=K, Rb) supports the C-type anti-ferro-orbital ordering.

A significant issue here to deal with is whether the SOC ruins the observed orbital ordering in $AMnF_4$ (A=K, Rb). To address this issue, we analyzed the orbital ordering phenomena when SOC was included. We found that the orbital ordered ground state remains robust (not shown here) upon inclusion of SOC in the system. This is consistent with the SOC effects in the electronic details due to the presence of the $3d$ Mn ion.

IV. CONCLUSION

Based on density functional theory, we analyzed the electronic, magnetic, and orbital ordering of the layered perovskite-type structures $AMnF_4$ (A=K, Rb) under the scheme of GGA+U. We observed that $AMnF_4$ (A=K, Rb) stabilizes in the FM ground state. Both compounds exhibit quasi-2D magnetism, with weak interaction between the layers. The corresponding critical temperatures are estimated to be around 30–60 K. However, the experimental reports suggest noncollinear and collinear AFM magnetic orders in both compounds. We have examined the effect of local Coulomb interaction in the $3d$ Mn shell, but the magnetic ground state and electronic structure properties remain unaffected by these factors. This discrepancy warrants further refinement of experiments observing AFM ordering and might indicate insufficiency of our theory level, which motivates further studies.

We spotted interesting nodal-line-like dispersions in these two structures at an energy range of 0.4 eV below the Fermi level. Such dispersion in Mott insulators may not have great significance, but one can look into band engineering possibilities through doping/pressure, which could lead to novel applications in the field of topologically nontrivial matter. Furthermore, we found that in both compounds, an anti-ferro-orbital ordering of $d_{x^2-y^2}$-like orbitals within the ab plane and a ferro-orbital ordering out of plane were observed, favoring C-type orbital ordering. The presence of the nodal-like dispersion, orbital ordering, and 2D-like magnetism in these compounds might increase the research interest in these fields.

ACKNOWLEDGMENTS

A.B. and V.K. would like to thank IIT Hyderabad and CDAC for providing computational resources. T.M. would like to thank IIT Roorkee for computational facilities. A.B. wishes to express her gratitude to Prof. G. S. Vaitheeswaran (School of Physics, University of Hyderabad) for fruitful discussions. A.B. would like to acknowledge DST-INSPIRE for providing her with a fellowship. V.K. would like to thank CSIR for funding under Reference No. 03(1433)/18/EMR-II. The work by A.N.R. is supported by the European Research Council via Synergy Grant No. 854843 - FASTCORR.

APPENDIX

1. Details of optimization and convergence tests

We provide the details of the optimized lattice parameters of $AMnF_4$ (A = K, Rb) in Tables IV and V respectively along with the convergence of exchange interactions performed for $KMnF_4$ as shown in Fig. 10.

TABLE IV. Optimized lattice parameters of $KMnF_4$ calculated with different exchange-correlation functionals.

	a (Å)	b (Å)	c (Å)	β
Expt.	7.68	7.63	5.74	90.40
PBE without U	7.87	7.84	5.88	90.65
PBE with U (= 3 eV)	7.88	7.84	5.89	90.68
PBE with U (= 5 eV)	7.86	7.81	5.92	90.68
PS without U	7.71	7.67	5.75	90.57
PS with U (= 3 eV)	7.73	7.68	5.77	90.61
PS with U (= 5 eV)	7.72	7.66	5.79	90.81
LDA without U	7.55	7.49	5.56	90.40
LDA with U (= 3 eV)	7.57	7.50	5.57	90.41
LDA with U (= 5 eV)	7.57	7.50	5.59	90.44

TABLE V. Optimized lattice parameters of $RbMnF_4$ calculated with different exchange-correlation functionals.

	a (Å)	b (Å)	c (Å)	β
Expt.	7.79	7.74	5.99	90.48
PBE without U	7.96	7.94	6.12	90.81
PBE with U (= 3 eV)	7.98	7.95	6.13	90.84
PBE with U (= 5 eV)	7.97	7.93	6.16	90.81
PS without U	7.80	7.77	5.99	90.67
PS with U (= 3 eV)	7.82	7.78	6.00	90.74
PS with U (= 5 eV)	7.82	7.78	6.02	90.72
LDA without U	7.64	7.58	5.82	90.56
LDA with U (= 3 eV)	7.66	7.61	5.87	90.66
LDA with U (= 5 eV)	7.66	7.60	5.84	90.66

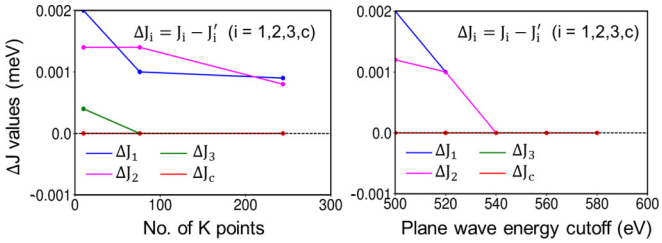

FIG. 10. The convergence of exchange interactions is verified by plotting relative J values (ΔJ) as a function of the number of k points and the plane-wave energy cutoff for $KMnF_4$ using PBE+U (U = 3 eV). Here, $\Delta J_i = J_i - J_i'$ ($i = 1, 2, 3, c$), where J_i' represents the values obtained with the finest grid (left panel) and the largest energy cutoff (right panel).

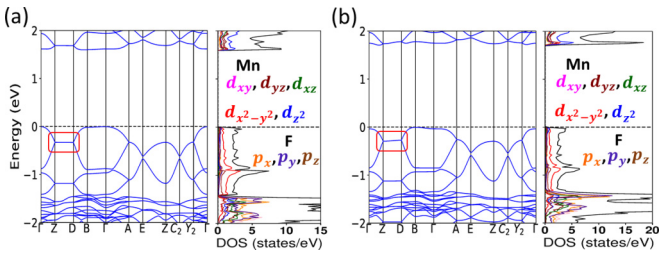

FIG. 11. Electronic band structures of $KMnF_4$ (left) and $RbMnF_4$ (right) when SOC is included along with the PDOS highlighting the predominant contribution of Mn d and F p states close to the Fermi level E_F.

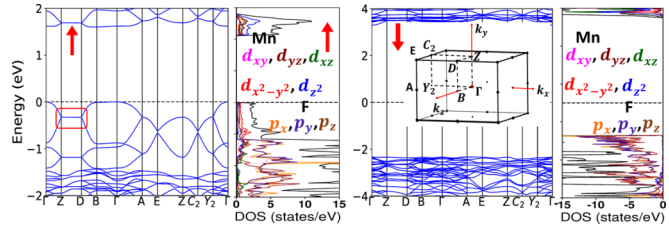

FIG. 12. Spin-polarized electronic band structure of $KMnF_4$ calculated using PBE+U (U = 5 eV) along the high-symmetry points as illustrated in the irreducible Brillouin zone (shown in the inset) and the PDOS highlighting the predominant contribution of Mn d and F p states close to the Fermi level E_F. Left: spin-up channel. Right: spin-down channel.

2. Electronic band structure when SOC is incorporated in the system, $AMnF_4$ (A = K, Rb)

Figure 11 shows the electronic band structures of $KMnF_4$ and $RbMnF_4$ when SOC is included.

3. Electronic band structure using PBE+U (U = 5 eV)

Figures 12 and 13 illustrates the spin-polarized electronic band structure of $KMnF_4$ and $RbMnF_4$ calculated using PBE+U respectively.

4. Details of the partial density of states of $RbMnF_4$

Figure 14 shows the calculated PDOS projected onto the 3d orbitals of four different Mn ions.

5. Details of the projected band structure and the 3D band dispersion of $RbMnF_4$

Figure 15 shows the calculated orbital-projected band structure in the spin-up channel for $RbMnF_4$ and illustrates the nodal line along the selected band paths.

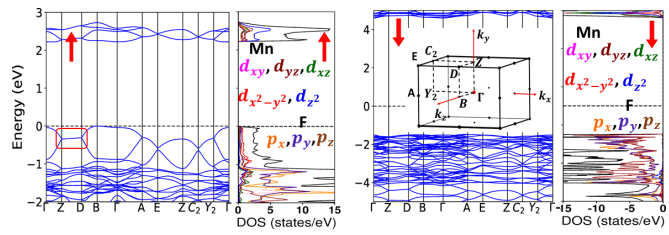

FIG. 13. Spin-polarized electronic band structure of $RbMnF_4$ calculated using PBE+U (U = 5 eV) along the high-symmetry points as illustrated in the irreducible Brillouin zone (shown in the inset) and the PDOS highlighting the predominant contribution of Mn d and F p states close to the Fermi level E_F. Left: spin-up channel. Right: spin-down channel.

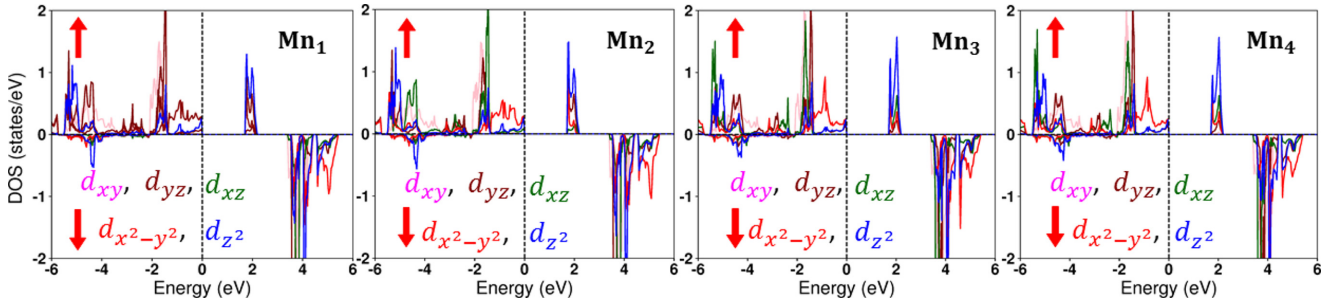

FIG. 14. Calculated PDOS projected onto the 3*d* orbitals of four different Mn ions in the ground state (FM structure) of $RbMnF_4$. Upward arrows (↑) indicate the spin-up channel, and downward arrows (↓) indicate the spin-down channel.

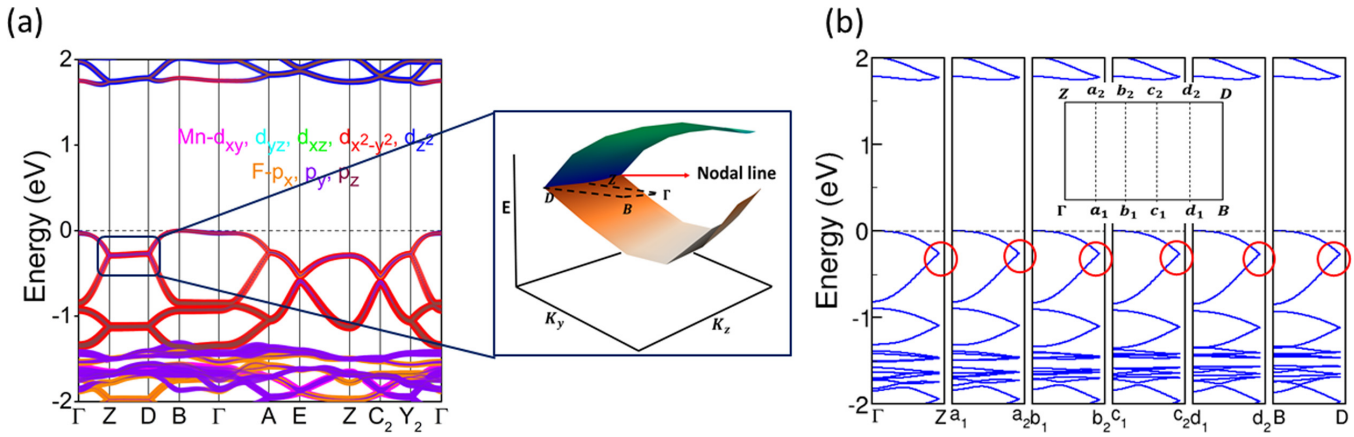

FIG. 15. (a) Calculated orbital-projected band structure in the spin-up channel for $RbMnF_4$ along with the 3D band representation of the nodal line (highlighted in the blue box). (b) Illustration of the nodal line along the selected band paths between Γ-*Z* and *B*-*D* (i.e., along the $k_x = 0$ plane).

[1] Y. Moritomo, A. Asamitsu, H. Kuwahara, and Y. Tokura, Nature (London) **380**, 141 (1996).

[2] A. Sotnikov, N. Darkwah Oppong, Y. Zambrano, and A. Cichy, Phys. Rev. Research **2**, 023188 (2020).

[3] P. Khalifah, R. Osborn, Q. Huang, H. W. Zandbergen, R. Jin, Y. Liu, D. Mandrus, and R. J. Cava, Science **297**, 2237 (2002).

[4] B. Keimer, Nat. Mater. **5**, 933 (2006).

[5] K. Ishigaki, J. Nasu, A. Koga, S. Hoshino, and P. Werner, Phys. Rev. B **99**, 085131 (2019).

[6] T. A. Miller, R. W. Chhajlany, L. Tagliacozzo, B. Green, S. Kovalev, D. Prabhakaran, M. Lewenstein, M. Gensch, and S. Wall, Nat. Commun. **6**, 8175 (2015).

[7] Y. Tokura and N. Nagaosa, Science **288**, 462 (2000).

[8] J. Varignon, M. N. Grisolia, D. Preziosi, P. Ghosez, and M. Bibes, Phys. Rev. B **96**, 235106 (2017).

[9] J. Varignon, M. Bibes, and A. Zunger, Nat. Commun. **10**, 1658 (2019).

[10] H. Chen, D. P. Kumah, A. S. Disa, F. J. Walker, C. H. Ahn, and S. Ismail-Beigi, Phys. Rev. Lett. **110**, 186402 (2013).

[11] E. Pavarini and E. Koch, Phys. Rev. Lett. **104**, 086402 (2010).

[12] E. Pavarini, E. Koch, and A. I. Lichtenstein, Phys. Rev. Lett. **101**, 266405 (2008).

[13] S. Margadonna and G. Karotsis, J. Mater. Chem. **17**, 2013 (2007).

[14] S. Margadonna and G. Karotsis, J. Am. Chem. Soc. **128**, 16436 (2006).

[15] C. Brosset, Z. Anorg. Allg. Chem. **235**, 139 (1937).

[16] C. Brosset, Z. Anorg. Allg. Chem. **239**, 301 (1938).

[17] M. C. Moron, F. Palacio, and J. Rodriguez-Carvajal, J. Phys.: Condens. Matter **5**, 4909 (1993).

[18] F. Palacio, M. Andres, C. Esteban-Calderon, M. Martinez-Ripoll, and S. Garcia-Blanco, J. Solid State Chem. **76**, 33 (1988).

[19] M. Morón, F. Palacio, and J. Rodriguez-Carvajal, Phys. B (Amsterdam, Neth.) **180–181**, 125 (1992).

[20] M. Molinier, C. Frommen, W. Massa, J. Pebler, and T. Roisnel, Z. Naturforsch. A **48**, 1054 (1993).

[21] P. E. Blöchl, Phys. Rev. B **50**, 17953 (1994).

[22] G. Kresse and J. Furthmüller, Comput. Mater. Sci. **6**, 15 (1996).

[23] G. Kresse and D. Joubert, Phys. Rev. B **59**, 1758 (1999).

[24] S. L. Dudarev, G. A. Botton, S. Y. Savrasov, C. J. Humphreys, and A. P. Sutton, Phys. Rev. B **57**, 1505 (1998).

[25] H. J. Zhao, X. Q. Liu, X. M. Chen, and L. Bellaiche, Phys. Rev. B **90**, 195147 (2014).

[26] V. Zhandun and A. Nemtsev, Mater. Chem. Phys. **259**, 124065 (2021).

[27] A. Smiri, S. Jaziri, S. Lounis, and I. C. Gerber, Phys. Rev. Materials **5**, 054001 (2021).
[28] W. Nolting and A. Ramakanth, *Quantum Theory of Magnetism* (Springer, Berlin, 2009)
[29] N. D. Mermin and H. Wagner, Phys. Rev. Lett. **17**, 1133 (1966).
[30] J. Rusz, I. Turek, and M. Diviš, Phys. Rev. B **71**, 174408 (2005).
[31] P. W. Anderson, Phys. Rev. **79**, 350 (1950).
[32] J. Kanamori, J. Phys. Chem. Solids **10**, 87 (1959).
[33] H. Weihe and H. U. Güdel, Inorg. Chem. **36**, 3632 (1997).
[34] D. I. Khomskii, *Transition Metal Compounds* (Cambridge University Press, Cambridge, 2014).
[35] I. V. Kashin, V. V. Mazurenko, M. I. Katsnelson, and A. N. Rudenko, 2D Mater. **7**, 025036 (2020).
[36] A. Behatha, A. J. Roy, C. V. Anusree, L. Ponvijayakanthan, V. K. Sharma, and V. Kanchana, J. Phys.: Condens. Matter **33**, 165803 (2021).